

1 Elucidating the role of soil hydraulic properties on aspect-dependent landslide initiation

2 Yanglin Guo^{1,2}, Chao Ma^{1,2}

3 1. School of Soil and Water Conservation, Beijing Forestry University, Beijing 100083, PR China.

4 2. Jixian National Forest Ecosystem Observation and Research Station, CNERN, Beijing Forestry University,
5 Beijing 100083, PR China.

6 Corresponding Author: Professor Chao Ma, sanguoxumei@163.com

7 **Abstract:** Aspect-dependent landslide initiation is an interesting finding, and previous studies have attributed this to
8 the mechanical effects of plant roots. In the present study, an overwhelming landslide probability on a south-facing
9 slope over a north-facing slope was found in a localized area with only granite underneath and high cover of *Larix*
10 *kaempferi*. These observations cannot be attributed to plant roots but may result from factors related to hillslope
11 hydrology. Differential weathering associated with hillslope hydrology behaviors such as rainfall water storage and
12 leakage, pore-water pressure, particle component, and hillslope stability fluctuation were used to examine these
13 observations. Remote sensing interpretation using the high-resolution GeoEye-1 image, digitalized topography and
14 field investigations showed that landslides on south-facing slopes have a higher probability, larger basal area, and
15 shallower depth than those on a north-facing slope. The lower limits of the upslope contributing area and slope
16 gradient condition for south-facing landslides were less than those for north-facing landslides. The higher basal areas
17 of south-facing landslides than those of the north-facing landslides may be attributed to the high peak values and
18 slow dissipation of pore-water pressure. The absorbed and drained water flow in given time interval, together with
19 the calculated water storage and leakage during the measured rainy season measured, demonstrate that the soil mass
20 above the failure zone for south-facing slopes is more prone to pore-water pressure, which results in slope failures.
21 In comparison, the two stability fluctuation results from the finite and infinite models further verified that landslides
22 on south-facing slopes may fail under conditions of prolonged antecedent precipitation and intensive rainfall.
23 Meanwhile, those on north-facing slopes may fail only in response to intensive rainfall. The results of this study will
24 deepen our knowledge of aspect-dependent landslide initiation from both classical mechanics and the state of stress.

25 **Keywords:** Landslide; Pore-water pressure; suction stress; Hydraulic conductivity; Slope stability

26 1 Introduction

27 In some semi-arid environments of the Northern Hemisphere, aspect-dependent landslide initiation provides
28 valuable insights into the relative importance of different factors in developing accurate landslide susceptibility
29 models (Ebel, 2015; Rengers et al., 2016; Li et al., 2021; Deng et al., 2022). These events provide a thorough
30 understanding of the amount of direct sunlight that translates into differences in vegetation communities, bedrock
31 weathering, and soil development processes (Fu, 1983; Wang, 2008; Bierman and Montgomery, 2014). These earth
32 surface processes indirectly affect hillslope hydrology and landscape dissection at the hillslope scale. Rainfall-
33 induced shallow landslides are geomorphic agents at the hillslope scale and are governed by multiple factors,
34 including hydrology, hillslope materials, bedrock, and vegetation (Birkeland, 1999; Geroy et al., 2011; Lu and Godt,
35 2013). Currently, the aspect-dependent landslide initiation observed has been predominantly attributed to the
36 mechanical effect of plant roots. This is because the differences in vegetation on the south- and north-facing slopes
37 are easier to examine and more pronounced than other factors (Li et al., 2021; Timilsina et al., 2021; Dai et al., 2022;
38 Deng et al., 2022). However, vegetation succession takes place over substantially longer timescales than soil
39 development and bedrock weathering (Watakabe and Matsushi, 2019). In most cases, the plant roots are not deep
40 enough to penetrate the bedrock (Schwinning, 2010). Hypothesizing for a relatively localized area with the same
41 ecosystem or plant species, aspect-dependent landslide initiation cannot be attributed to plant roots but may result
42 from differences in the properties of hillslope materials due to long-term differential weathering.

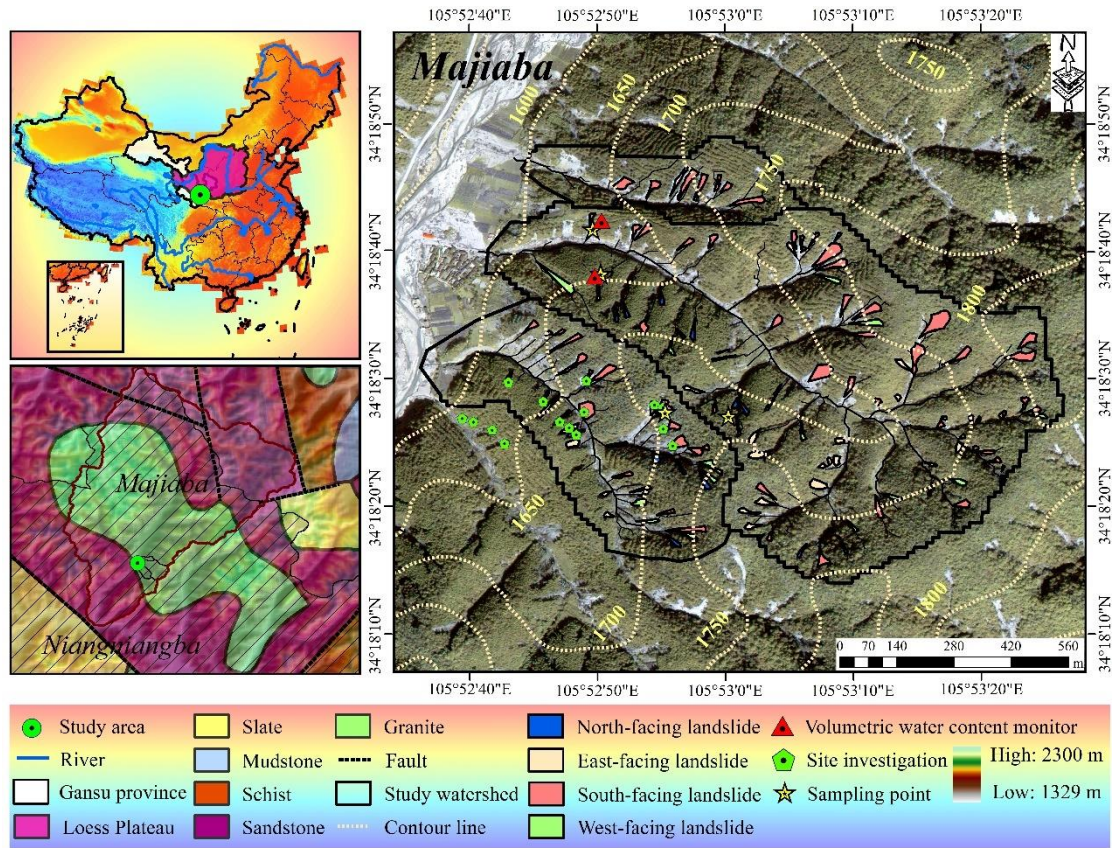
43 Aspect-dependent landslides in Frontal Colorado, USA and the Loess Plateau, China, have attracted interest
44 because vegetation has a considerable influence on landslide distribution. The strong propensity for shallow landslide
45 initiation on south-facing hillslopes in the two regions is closely related to the present-day tree density, regardless of
46 the hillslope aspect (Ebel, 2015; Rengers et al., 2016; Deng et al., 2022). In the Colorado Frontal Range, field
47 observations have shown that south-facing slopes lack thick tree cover and have an abundance of rock outcrops
48 compared to north-facing slopes. In addition, the soil layer is thinner on south-facing slopes (Coe et al., 2014; Ebel
49 et al., 2015). The cohesion supplied by the roots is responsible for the connection observed between landslide
50 distribution and slope aspect (McGuire et al., 2016). On the Loess Plateau, vegetation recovery is one of the main
51 ecological measures for mitigating sediment loss (Fu et al., 2009). Increased soil strength and hydraulic conductivity
52 due to strong root networks may enhance the topographic initiation conditions (Montgomery and Dietrich, 1994;
53 Wang et al., 2020). North- and westward moving storms may potentially produce more intense rainfall on the south-
54 and east-facing slopes. This assumption may be invalid if an aspect-dependent landslide distribution is present in a
55 localized catchment with a specific vegetation community. This study highlights the effect of the mechanical function
56 of plants on landslides. If an aspect-dependent landslide exists in a localized area with vegetation cover comprising
57 the same plant species alongside a high level of vegetation cover, the aspect-dependent landslide initiation observed
58 cannot be attributed to the mechanical effect of plant roots.

59 To determine the relationship observed among vegetation, landslides, and slope aspect, the effects of the
60 physical properties and strength of hillslope materials cannot be excluded. On the northern part of the Loess Plateau,
61 China, as well as in many other semi-arid environments, different types and densities of vegetation and soils develop
62 on north-facing versus south-facing convergent slopes (Fu, 1983; Heimsath et al., 1997; Wang, 2008). This is because
63 systematic differences in the amount of direct sunlight translate into differences in physical and chemical weathering.
64 North-facing convergent slopes have lower evaporation rates, retain snow cover longer in spring, and tend to hold
65 soil moisture longer during the summer growing season. These differences may result in localized ecosystem
66 communities in the presence of trees or shrubs on grass. South-facing slopes experience heavier and more frequent
67 hydration, thermal expansion, or freeze-thaw cycles due to day warming and night cooling and tend to have stronger
68 weathering throughout the year. These differences can result in local differences in the grain component, soil strength,
69 and soil profile. This has indirect effects at the landslide scale through the mechanics of excessive pore-water
70 pressure dissipation and sliding surface liquefaction (Terzaghi, 1950; Sassa, 1984), and hillslope hydrology behavior
71 (Godt et al., 2009; Lee and Kim, 2019). Therefore, the physical properties of hillslope materials may be attributed
72 to the aspect-dependent landslide initiation observed.

73 Shallow landslides are examples of debris flow initiation, which often enlarges their scale by multiple
74 mechanics (Hungr et al. 2005; Iverson et al. 2011). When the slope fails, the pore-water pressure abruptly increases
75 within the shear zone (Iverson and LaHusen, 1989; Wang and Sassa, 2003). If the excessive pore-water pressure
76 persists high over the static pressure for a relatively long duration, the displaced masses enlarge their volume by
77 widespread liquefaction and transform into debris flows (Bogaard and Greco, 2016). The magnitude of the pore-
78 water pressure is closely related to the scale of the shallow landslide. Therefore, the scale of shallow landslides can
79 be determined by excessive pore-water pressure during the failure process. However, the aspect-dependent landslide
80 distribution in these two areas refers to the differences in landslide probability rather than the landslide scale.

81 In the present study, we used a combination of field soil moisture observation, strength measurement, hydraulic
82 conductivity analysis of hillslope materials, and numerical modeling of slope stability to explain the high potential
83 for landslide initiation on south-facing slopes relative to north-facing slopes with the same vegetation communities.
84 Differences in landslide geometry and initiation conditions, in the form of the contributing area above the scar area
85 and the landslide gradient, were shown using field studies and high-resolution GeoEye-1 images. The differential
86 weathering-related physical properties and strength of the soil mass, including the dry unit weights, porosity, grain

87 size, effective cohesion, and inner friction angle were examined. We have also highlighted the importance of
 88 excessive pore-water pressure, hillslope hydrology, and stability in explaining the aspect-dependent landslide
 89 initiation observed. The results of this work will deepen our understanding of aspect-dependent landslide distribution
 90 in some mountainous areas of the Northern Hemisphere.



91
 92 **Fig. 1.** Location, topography, and simplified lithology of the study area. All maps are created by the authors. The
 93 graph of Majiaba was taken using an Unmanned Aerial Vehicle. The territorial domain of China and simplified
 94 lithology map are from China Geological Survey. Elevation legend refers to the mountain spanning
 95 Niangniangba and Majiaba.

96 **2 Study area**

97 The study area is in the mountainous region of Majiaba village, northeast of Niangniangba town, Tianshui City,
 98 Gansu Province, Central China. It is also close to the dividing crest of the Yellow and Yangtze Rivers and on the
 99 eastern part of the Loess Plateau. The elevation of the mountain near Niangniangba town in the mountain region of
 100 the study area ranges from 1329 m to 2300 m. Most of the hillslope is underlain by sandstone, and the stratigraphic
 101 units of granite, slate, schist and mudstone account for a smaller area. This area has four distinctive seasons and a
 102 semi-humid climate. The annual precipitation is approximately 491.6 mm and predominantly falls during June and
 103 August. One branch fault of the Tianshui-Lanzhou fault system runs through the area and has had no rupture records
 104 for the last few decades.

105 The shallow landslides in the study area and nearby surroundings were triggered by the prolonged antecedent
 106 precipitation during July 1–24 and the intensive rainstorm on July 25, 2013 (Yu et al., 2014; Guo et al., 2015). Most
 107 shallow landslides in the entire storm spanned the mountain area with a gradient of 20–25 °, located on south-facing
 108 slopes and in areas with relatively low-coverage vegetation (Li et al., 2021). Besides, some works found that plant
 109 roots may increase the topographical initiation threshold of landslides because of their positive effect on the strength

110 and hydraulic conductivity of soil-root composite (Dai et al., 2022). The three small catchment areas in the Majiaba
111 Watershed are underlain by granite units. The total area is 0.88 km² with vegetation cover of over 90% (Fig. 1). The
112 relative relief was approximately 200 m, and the mean hillslope gradient was 37°. The reason why the three
113 catchments in the area were chosen is that the main plant species on the south- and north-facing slope is *Larix*
114 *kaempferi*, which commonly have highly developed lateral roots with depth < 0.4 m. However, landslides in the
115 three catchments still have a higher propensity for occurrence on south-facing slopes in comparison with the north-
116 facing slopes. This finding differs from the results from Frontal Range, Colorado, USA, and the Central Loess
117 Plateau, where landslides commonly occur in sparsely vegetated areas. Li et al. (2021) only addressed the
118 relationship between landslide probability and vegetation cover at the regional scale, while excluding the importance
119 of the properties of hillslope materials at a more localized scale. Therefore, we hypothesize that such observations
120 in the study area may not be the result of the mechanical effect of plant roots but may be from the distinctive physical
121 properties and strength of hillslope materials due to differential weathering.

122 **3 Materials and methods**

123 **3.1 Landslide information interpretation**

124 The high resolution GeoEye-1 image (0.5 m × 0.5 m) on October 8, 2013 was orthorectified and the landslide
125 boundary was visually interpreted using ENVI 5.1 and e-Cognition 8. An unmanned aerial vehicle (UAV) was used
126 to obtain a digital elevation model (DEM) with a 5 m resolution. The GeoEye-1 orthographic image and DEM were
127 spatially registered in ArcGIS 10.2 as a standard layer of orthoimage. The landslide initiation condition is represented
128 by the competition between the slope gradient and upslope contribution area ($A-S$):

$$129 \quad S = kA^{-b} \quad (1)$$

130 where S is the local slope (m/m); A is the contribution area above the landslide head scar (m²); k is an empirical
131 constant related to lithology, vegetation, and climate; and b is an empirically defined index.

132 Field studies were conducted to measure the depth of the head scar and sidewall area using tape, and the failure
133 depth was taken as their average. The landslide volume could then be calculated using the interpreted scar area and
134 failure depth measured. Detailed landslide information including the landslide number and area probability, landslide
135 volume and width, head scar and sidewall depth, and the upslope contributing area–slope gradient condition for the
136 south- and north-facing slopes were compared.

137 **3.2 Field monitoring and soil sampling**

138 To investigate the hillslope hydrology on south- and north-facing slopes, Frequency Domain Reflectometry
139 (FDR) soil moisture sensors were used in this work to record the volumetric water content. To avoid the randomness
140 of data caused by natural factors such as terrain and vegetation, a total of 16 shallow landslides were investigated to
141 excavate soil profiles and take undisturbed soil samples. Sensors were installed at depths of 30 cm, 70 cm, and 110
142 cm on the south- and north-facing slopes to monitor the volumetric water content during June and September 2021.
143 Soil moisture monitoring was implemented at two concave sites on the south- and north-facing slopes. The
144 meteorological station was less than 3 km away from the study area to record the rainfall on a 30 min basis. During
145 the sensor installation, undisturbed soil samples near the sensor location were taken for indoor tests, including the
146 dry unit weight, porosity, grain size, shear strength, and hydraulic conductivity. The grain size was analyzed using a
147 Malvern MS 3000 instrument (Malvern, England). In each layer, at least four samples were collected for the
148 consolidated undrained triaxial compression test (CU). Two samples were collected for unsaturated hydraulic
149 conductivity measurement using transient release and imbibition tests (Lu and Godt, 2013). Saturated hydraulic
150 conductivity was determined using the constant water head method (Table 1).

151 **3.3 Pore-water pressure dissipation**

152 CU tests were performed to obtain the effective cohesion, effective internal friction angle, and pore-water

153 pressure curves. Soil samples with a diameter of 50 mm and height of 100 mm were first saturated in a vacuum
 154 pump. They were then consolidated in the chamber of the GDS apparatus at 50, 100, 150, and 200 kPa confining
 155 pressures and 10 kPa backpressure. During each test, the shearing rate was set to 0.1 mm/min, and the device
 156 automatically recorded data every 10 s. Owing to the varied particle components and soil texture, the increasing and
 157 dissipation ratios of pore-water pressure differentiate a lot. As a high excessive pore-water pressure and slow
 158 dissipation ratio could cause widespread Coulomb failure within the shear zone, it will influence the landslide scale.
 159 To compare the rate of rise and dissipation of pore-water pressure during the CU test, the ratio is expressed as

$$160 \quad i = \frac{p_{t+\Delta t} - p_t}{\Delta t} \quad (2)$$

161 where i is the increase or dissipation ratio of the excessive pore-water pressure, and p_t and $p_{t+\Delta t}$ are the pore-water
 162 pressures measured during the time interval of Δt . A higher i indicates that the pore-water within soil mass drainage
 163 rapidly and the pore-water pressure will dissipate in a short time. In other words, the i is a proxy representing the
 164 hydraulic conductivity.

165 3.3 Water storage and drainage

166 The unsaturated permeability of soil mass (diameter 61.8 mm, height 25.4 mm) was measured using the
 167 Transient Release and Imbibition method (TRIM) (Lu and Godt, 2013). In this test, the water outflow mass was
 168 measured on a 10 min basis. In each test, air pressures of 250 kPa and 0 kPa corresponded to the drying and wetting
 169 processes, respectively. The Soil Water Characteristic Curve (SWCC) and Hydraulic Conductivity Function (HCF)
 170 were obtained using Hydrus 1-D (Wayllace and Lu, 2012). Using the models proposed by Mualem (1976) and van
 171 Genuchten (1980), the constitutive relations between the suction head (h), water content (θ), and hydraulic
 172 conductivity (K) under drying and wetting states can be represented by the following equation:

$$173 \quad \frac{\theta - \theta_r}{\theta_s - \theta_r} = \left[\frac{1}{1 + (\alpha|h|)^n} \right]^{1 - \frac{1}{n}} \quad (3)$$

174 and

$$175 \quad K = K_s \frac{\left\{ 1 - (\alpha|h|)^{n-1} [1 + (\alpha|h|)^n]^{\frac{1}{n}-1} \right\}^2}{[1 + (\alpha|h|)^n]^{\frac{1}{2} - \frac{1}{2n}}} \quad (4)$$

176 where θ_r is the residual moisture content (%), θ_s is the saturated moisture content (%), α and n are empirical
 177 fitting parameters, α is the inverse of the air-entry pressure head, n is the pore size distribution parameter, and K_s
 178 is the saturated hydraulic conductivity (cm/s).

179 The soil water storage (S_s) and drainage (S_d) during a rainfall event can be evaluated by the soil depth and the
 180 difference between the maximum soil moisture and antecedent soil moisture:

$$181 \quad S_e = \frac{\theta - \theta_r}{\theta_s - \theta_r} \quad (5)$$

$$182 \quad S_s = S_e^w \Delta h \quad (6)$$

$$183 \quad S_d = P - S_e^d \Delta h \quad (7)$$

184 where S_e is the degree of saturation, θ is the volumetric moisture content measured (%), Δh is the average soil
 185 thickness (400 mm in this study), S_e^w and S_e^d are the residual soil moisture in the wetting and drying processes
 186 (%), and P is the accumulated rainfall (mm).

187 3.4 Stability fluctuation

188 In this study, we applied a finite and infinite stability model to assess the slope stability fluctuation during the
 189 rainy season as an attempt to examine aspect-dependent landslide initiation from the perspective of classical
 190 mechanics and the state of stress (Schmidt et al., 2001). The finite-slope model evaluates the stability F'_s :

$$191 \quad F'_s = \frac{c_l A_l + c_b A_b + A_b (\rho_s - \rho_w S_e) g z \cos^2 \beta \tan \phi'}{A_b \rho_s g z \sin \beta \cos \beta} \quad (8)$$

192 where β is the topographic slope angle ($^{\circ}$), A_l is the lateral area of side wall, m^2 , A_b is the basal area, m^2 , z is
 193 the sliding depth (m), c_l is the effective cohesion along the sidewall (kPa) and adopts the cohesion of layer 1 and
 194 layer 2, c_b is the basal soil cohesion (kPa), and adopts the cohesion of layer 3, ρ_s is the soil particle density, g/cm^3 ,
 195 and ρ_w is the water density, g/cm^3 .

196 The infinite slope stability model in this study provides insight into the stress variation resulting from changes
 197 in the soil suction and water content during infiltration (Lu and Likos, 2006):

$$198 \quad F_s'' = \frac{\tan \varphi'}{\tan \beta} + \frac{2c'}{\gamma z \sin 2\beta} - \frac{\sigma^s}{\gamma z} (\tan \beta + \cot \beta) \tan \varphi' \quad (9)$$

199 where φ' is the effective friction angle, $^{\circ}$; β is the topographic slope angle, $^{\circ}$; c' is the effective cohesion, kPa; γ
 200 is the unit weight of the soil, KN/m^3 ; and σ^s is the suction stress (kPa), expressed as:

$$201 \quad \sigma^s = -\frac{S_e}{\alpha} \left(S_e^{n/(1-n)} - 1 \right)^{1/n} \quad (10)$$

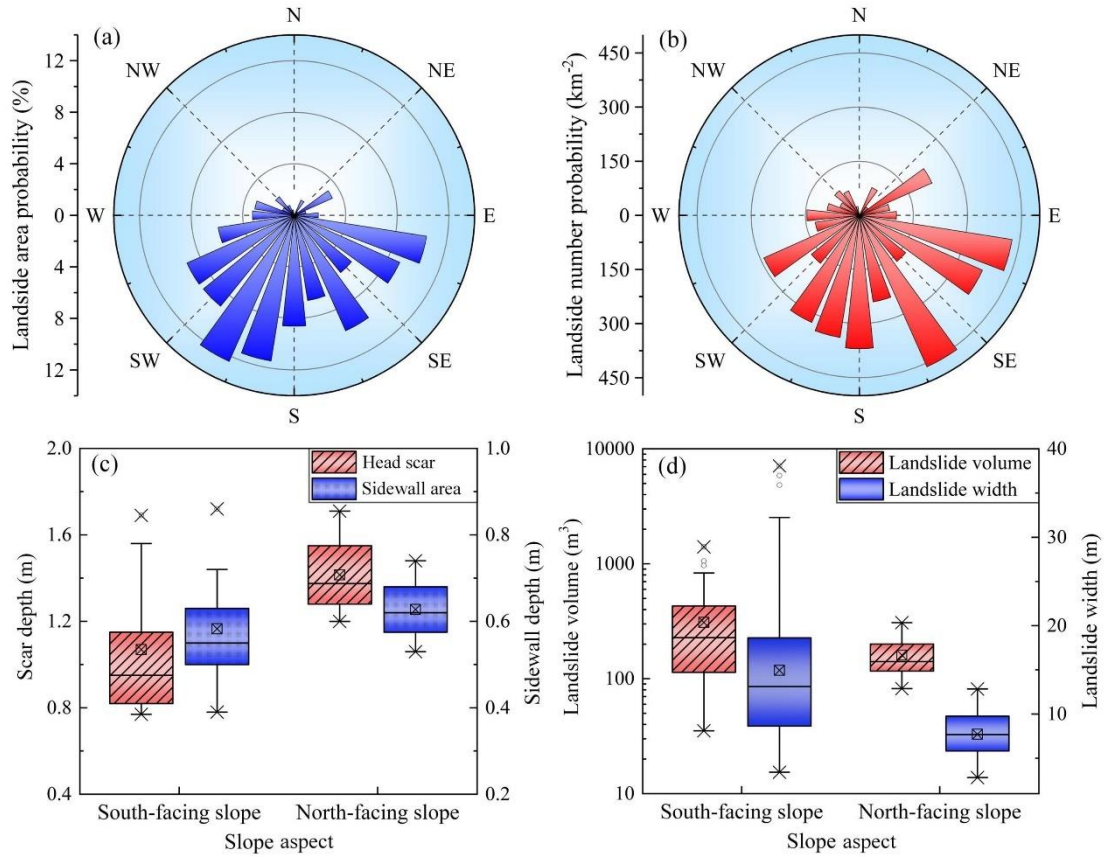
202 **4 Results**

203 **4.1 Shallow landslides on south- and north-facing slope**

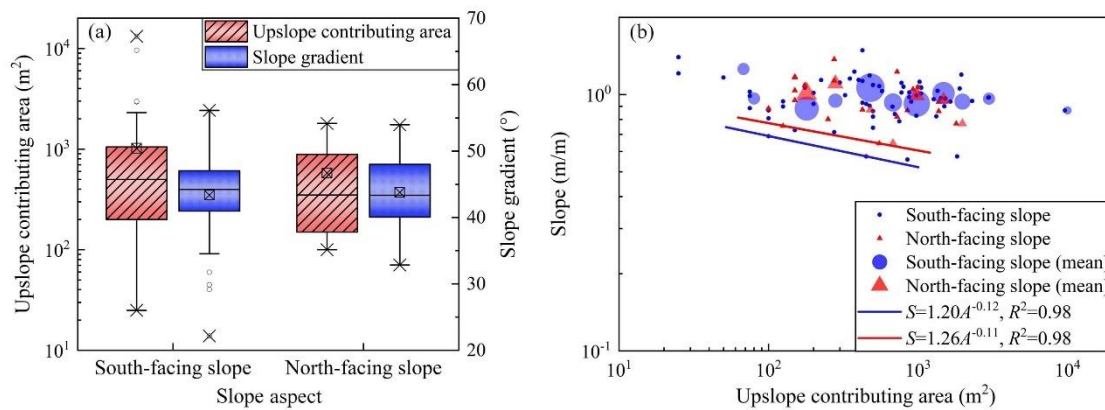
204 In the study area, the direct sunlight does not coincide with the aspect orientation because it is in the north the
 205 Tropic of Cancer. The south-facing slope is defined between 157.5° and 247.5° and the north-facing slope is between
 206 0° to 67.5° , and 292.5° to 360° (0° is the due north). There were 71 shallow landslides on the south-facing slope
 207 and 20 landslides on the north-facing slope in the study area. Figure 2a shows that shallow landslides on south-facing
 208 slopes have larger spatial areas than those on north-facing slopes. Most of the shallow landslides occurred on the
 209 south-facing slope (Fig. 2b). The volume of landslides on the south-facing slope was greater than that on the north-
 210 facing slope. For landslides on the south-facing slope, the basal area was $372.64 m^2$ and the width was $14.9 m$ on
 211 average. For landslides on the north-facing slope, the average basal area was $157.28 m^2$ and the width was $7.7 m$
 212 (Fig. 2c). Although the landslides on the south-facing slope had a larger volume and greater width, the depth of the
 213 head-scar and sidewall area are no greater than those on the north-facing slope. Field studies showed that the
 214 averaged depth for landslides on the north-facing slope was $1.02 m$, which was deeper than the depth of $0.83 m$ for
 215 landslides on south-facing slope (Fig. 2d). The landslides on the south-facing slope exhibited an overwhelming
 216 propensity for occurrence in terms of number and area. Meanwhile, the failure depth was no more than that of the
 217 landslides on the north-facing slope.

218 Shallow landslides can be modeled as occurring when sufficient through-flow converges from the upslope
 219 contribution area to the hollow area and triggers slope instability (Montgomery and Dietrich, 1994). Their
 220 topographic initiation conditions are controlled by the spatial competition between the slope and upslope contribution
 221 being area dependent (Stock and Dietrich 2003 and 2006; Horton et al., 2008). For the shallow landslides in the
 222 study area, the averaged upslope contributing area and slope gradient did not significantly differ (Fig. 3a). Meanwhile,
 223 the lower limit line representing the minimum initiation condition for landslides on south-facing slopes was lower
 224 than that on the north-facing slopes (Fig. 3b). This indicates that a higher upslope contribution area was required to
 225 provide sufficient through-flow conditions and trigger slope failures on the north-facing slope. Given that the
 226 landslides in the study area were triggered by prolonged antecedent precipitation and intensive rainfall (Li et al.,
 227 2021), sufficient rainfall infiltration could result in a high soil water content within the displaced mass, leading to a
 228 decrease in matric suction and soil strength. The generation of pore-water pressure in response to intense rainfall
 229 also plays an important role in shallow landslides. Therefore, we have proposed two assumptions to elucidate the
 230 distribution and scale of aspect-dependent landslides. The first assumption is that the basal area of the landslide may
 231 be related to the soil strength and high pore-water pressure. This assumption can be tested by the pore-water
 232 properties, including the pore-water generation potential and dissipation ratio during the failure process. The second

233 assumption is that the south-facing slope may have a higher failure potential than the north-facing slope in given
 234 rainfall process. This can be determined from the stability comparison using equations (8) and (9).



235
 236 **Fig. 2.** Spatial distribution and geometric characteristics of the landslide: (a) Landslide area probability vs slope
 237 aspect; (b) landslide number probability vs slope aspect; (c) landslide volume and width vs slope aspect; (d)
 238 scar depth and sidewall depth vs slope aspect. The edge line of box in the box chart shows the 75th quantile
 239 (Q3), median and 25th quantile (Q1) from top to bottom. The length of the box is referred to as the inter-quantile
 240 range (IQR). The crossed square inside the box is the average value. The whiskers extend to the maximum and
 241 minimum values except the mild outliers. The upper limit and lower limit of whiskers are $Q3+1.5IQR$ and $Q1-$
 242 $1.5IQR$ respectively. The circles are the outliers, and the cross symbol is the maximum and minimum values
 243 for all the data.



244
 245 **Fig. 3.** Upslope contributing area and slope gradient condition: (a) Upslope contribution area and mean slope vs
 246 slope aspect; and (b) the upslope contributing area vs mean slope gradient above the landslide area. The
 247 definitions of the whiskers are shown in caption of fig. 2. The circles are averaged slopes with the radius size

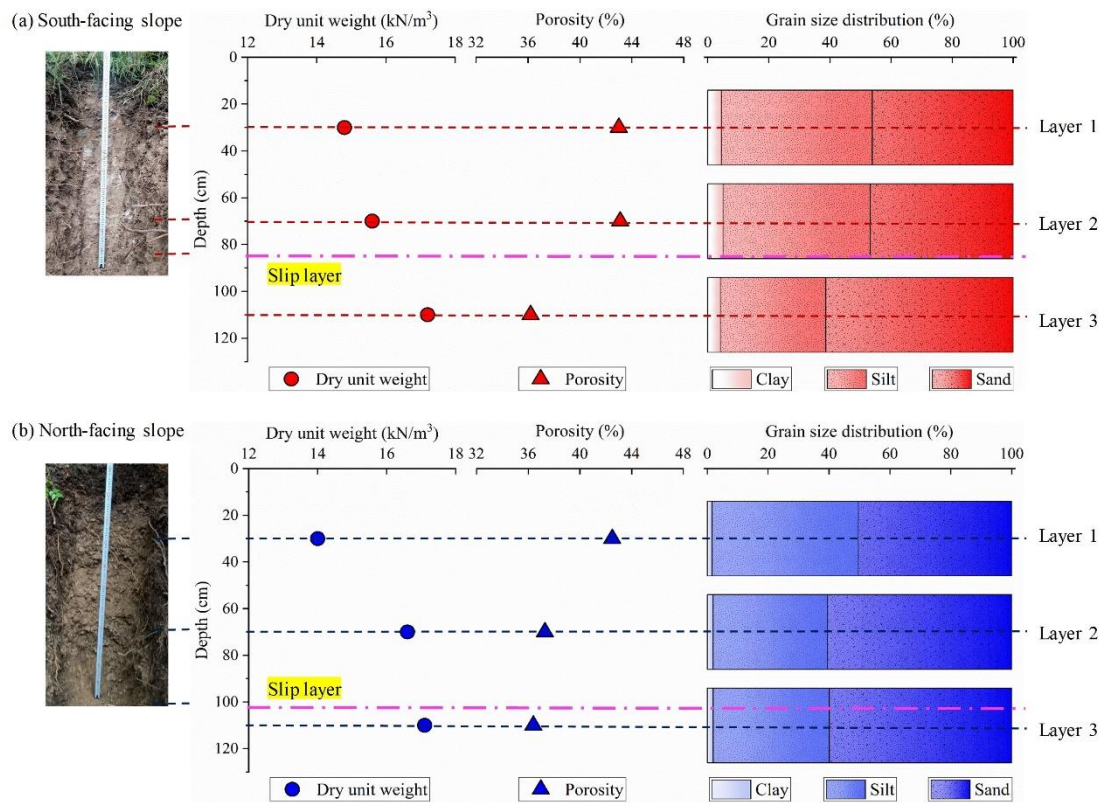
248 proportional to the number of landslides. The small cross represent all individual data values. The power-law
 249 regression is fitted with the dataset closet to the axis origin.

250 **4.2 Differences in soil physical properties**

251 To show the differences in the physical properties of the hillslope materials, the dry unit weights, porosity, and
 252 grain size distribution of the soil mass in the three layers on each slope were compared (Fig. 4). The effective
 253 cohesion and inner friction angle were then examined with respect to the particle component (Table 1 and Fig. 5).
 254
 255

Table 1 Physical properties and strength parameters of the soil mass

Parameters	South-facing slope			North-facing slope		
	Layer 1	Layer 2	Layer 3	Layer 1	Layer 2	Layer 3
Unit weight of soil (kN/m ³)	14.8	15.6	17.2	14	16.6	17.1
Porosity (%)	43.0	43.1	36.2	42.5	37.3	36.4
Effective cohesion (kPa)	6.5	17.5	21.2	5.3	9.1	7.9
Effective inner friction angle (°)	29.8	25	31	27.1	35.2	41
Saturated hydraulic conductivity (cm/s)	6.4×10 ⁻³	6.2×10 ⁻⁴	4.4×10 ⁻⁴	8.8×10 ⁻³	1.2×10 ⁻³	4.3×10 ⁻³

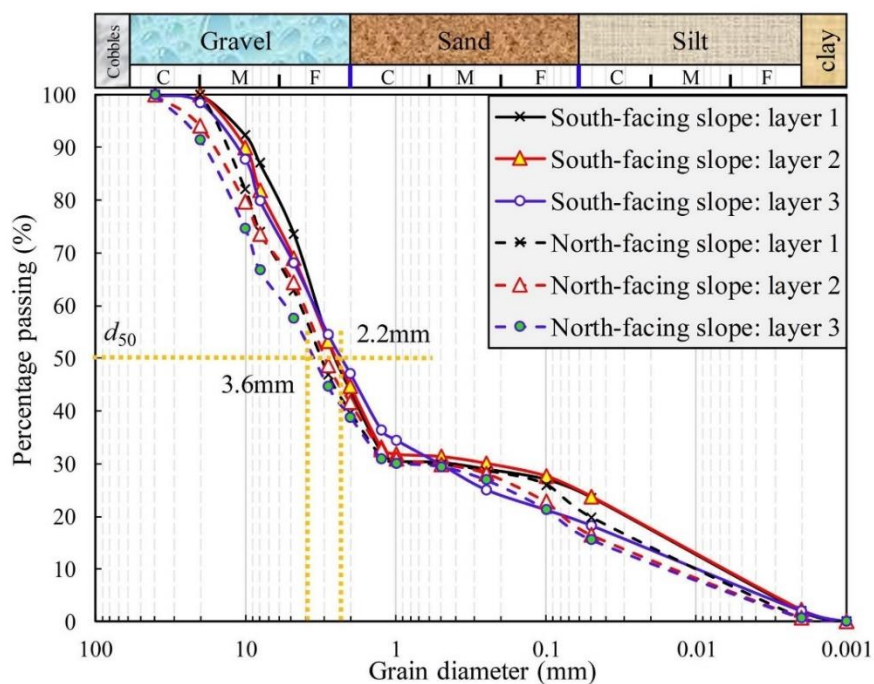


256
 257 **Fig. 4.** Differences in the soil properties including dry unit weights, porosity, and grain size in sand, silt, and clay.
 258 (a) Physical properties of soil mass on the south-facing slope; and (b) physical properties of soil mass on the
 259 north-facing slope. The two-soil profile photos were taken by Yanglin Guo during field studies.
 260

261 For the soil mass on the south-facing slope, the dry unit weights increased with soil depth, whereas the porosity
 262 and saturated hydraulic conductivity decreased (Fig. 4a and Table 1). For Soil layers 1 and 2, the soil textures were
 263 similar, because the proportions of sand, silt, and clay did not differ significantly. However, the proportion of silt in

264 Soil layer No. 3 was no more than that in layers No. 1 and 2, and the sand proportion was higher. The average failure
 265 depth was above Soil Layer No. 3 and below Soil Layer No. 2. For the soil mass on the north-facing slope, the dry
 266 unit weight also increased with soil depth. Unlike the south-facing slope, the porosity of the soil mass for the three
 267 soil layers was approximately 38% and did not differ among them. For the soil texture, the proportion of sand in Soil
 268 Layer No. 1 was no more than that in Soil Layers No. 2 and 3 (Fig. 4b). The depth of the failure plane was close to
 269 that of Soil Layer 3.

270 In comparison, one of the main difference was the higher saturated hydraulic conductivity for the soil mass
 271 above the failure plane on the north-facing slope. This may have resulted from the high porosity and sand proportion.
 272 This indicates that the rainfall infiltration on the north-facing slope could penetrate faster than that of the south-
 273 facing slope. The soil mass of the three layers on the south-facing slope had a higher proportion of fine particles than
 274 those on the north-facing slope if gravel was considered (Fig. 5). The saturated hydraulic conductivity for the soil
 275 masses from Soil Layers No. 2 and 3 on the south-facing slope was lower than that on the north-facing slope. This
 276 is expected because the porosity and proportion of fines on the south-facing slope were higher.



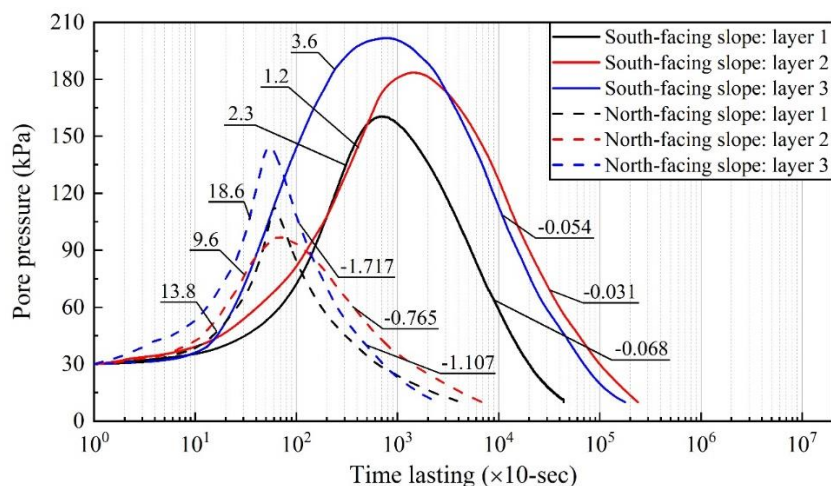
277
 278 **Fig. 5.** Soil particle component curves

279 According to the results of the triaxial shear test (Table 1), the soil mass in each layer on the north-facing slope
 280 had a smaller effective cohesion than that on the south-facing slope. The effective cohesion on the failure plane for
 281 landslides on the south-facing slope may be twice that on the north-facing slope. However, the effective inner friction
 282 angles for the soil masses of Soil Layers 2 and 3 on the north-facing slope were far greater than those on the south-
 283 facing slope. These differences in effective cohesion and inner frictional angle may be attributed to the higher clay
 284 and silt and fewer coarse grains within the soil mass on the south-facing slope.

285 **4.3 Pore-water pressure properties**

286 The consolidation module of the triaxial shear test was used to measure the generation and dissipation process
 287 of the pore-water pressure. The principle is to consolidate and drain soil from the initial saturated state. Under the
 288 same confining pressure, there are pronounced differences in the consolidation rate, consolidation time, and peak
 289 rise in pore-water pressure for different soil properties. The results of the pore-water pressure during the
 290 consolidation process under 200 kPa effective confining pressure were compared here (Fig. 6). The peak value of
 291 pore-water pressure within the soil mass on the south-facing slope was higher than that on the north-facing slope.

292 The peak value of the pore-water pressure within the soil mass on the south-facing slope increased to 150–200 kPa.
 293 However, the peak value of pore-water pressure within the soil mass on the north-facing slope was below 150 kPa.
 294 Both the rising and decaying rates of pore-water pressure for Soil Mass layers 1 and 2 on the south-facing slope were
 295 lower than those on the north-facing slope. The rate and decaying rates for Soil Mass layer No. 2 on the south-facing
 296 slope were 1.2 kPa/10 s and -0.031 kPa/10 s, respectively. However, they were 9.6 kPa/10 s and -0.765 kPa/10 s
 297 for the soil mass on the north-facing slope.



298
 299 **Fig. 6.** Variation in pore-water pressure under effective confining pressure of 200 kPa by GDS triaxial shear
 300 tests. The values in the figure 6 are the average rates of rise and dissipation of pore-water pressure during
 301 consolidation calculated by Equation 2. The unit of x-axis marks the time record interval of 10 seconds.
 302

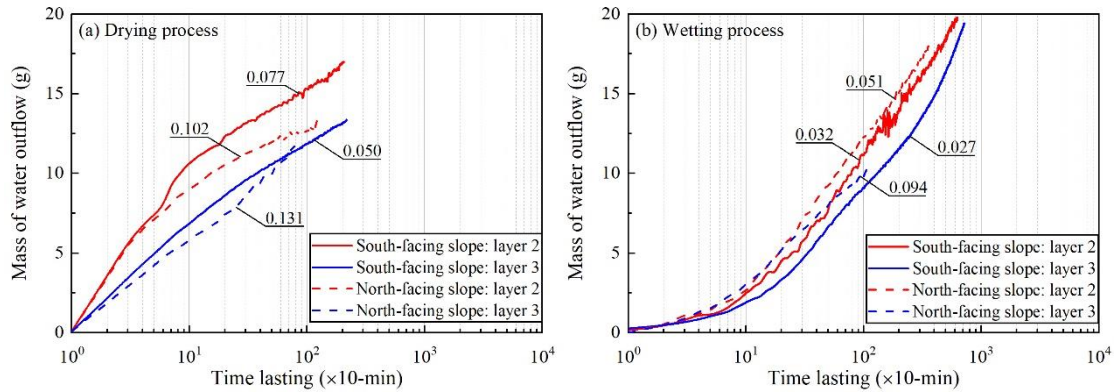
303 The lower peak pore-water pressure demonstrates the effect of fine particles on the pore-water pressure, which
 304 directly affects landslide mobility and scale. Rainfall-induced landslides result from an increase in positive pore-
 305 water pressure within the failure plane, which reduces the effective stress and shear strength of the soil (Terzaghi,
 306 1950). This often occurs in the undrained soil layer, which can easily cause slope liquefaction (Sassa, 1984). The
 307 increase in pore-water pressure predominantly depends on the speed of landslide movement, soil deformation, and
 308 soil permeability. If the shear rate is given, the dissipation rate of pore-water pressure for high-permeability soil is
 309 faster, and therefore, the increase in pore pressure is smaller (Iverson and LaHusen, 1989; Iverson et al., 1997). As
 310 shown in Table 1, the saturated hydraulic conductivity for soil mass of Layers No. 2 and 3 on the north-facing slope
 311 was 10 times that of the south-facing slope. Therefore, the peak pore-water pressure measured during the test for the
 312 soil mass on the south-facing slope was higher. The soil mass on the north-facing slope had higher sand and gravel
 313 contents than that on the south-facing slope (Fig. 5). A high clay content on the south-facing slope filled the
 314 macropores within the soil mass and reduced the pore-water discharge rate. Wang and Sassa (2003) found that fine
 315 particles play the most important role in the dissipation of pore pressure. The pore-water pressure within the saturated
 316 sand increased with shear rate. The soil mass with high coarse particles produced less pore water pressure than the
 317 soil with high fine particles during the shear process. Therefore, the high permeability of the soil mass on the north-
 318 facing slope may result in low peak-pore water pressure. The higher fine particles may result in a slow increase and
 319 dissipation of the pore-water pressure. This slow pore-water pressure dissipation could result in the liquefaction
 320 failure of the sliding mass and a larger landslide area.

321 4.4 Unsaturated hydraulic conductivity

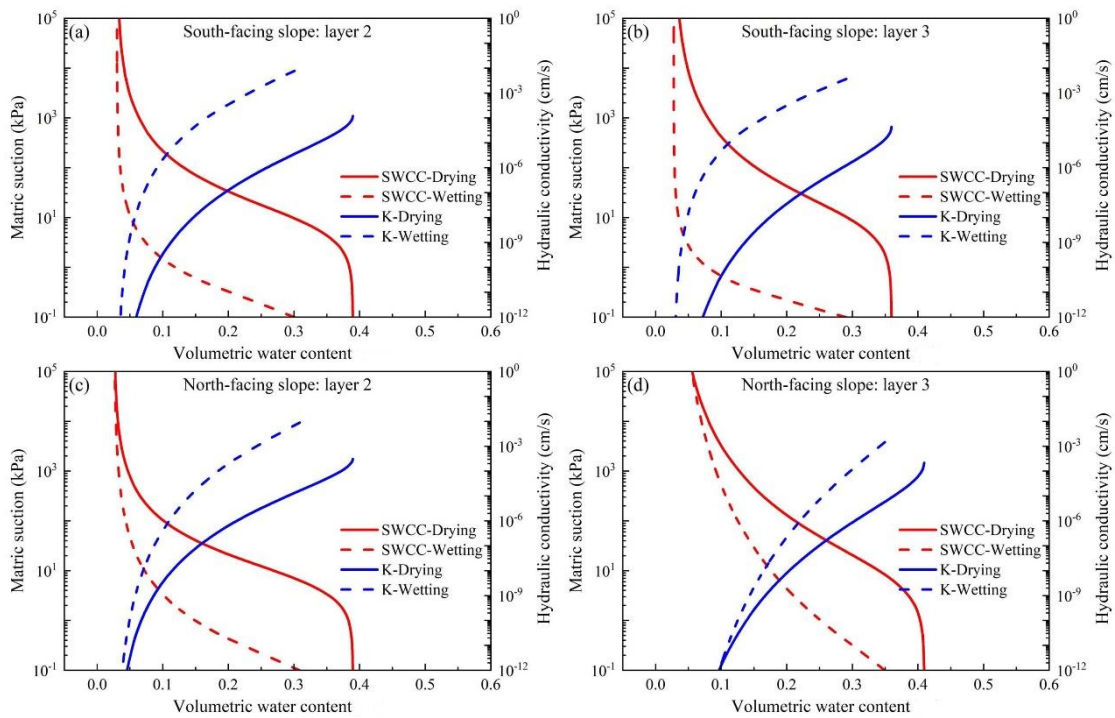
322 4.4.1 Measured water outflow mass

323 Figure 7 shows the water outflow mass measured for a given 10 min period during the drying and wetting
 324 processes. The water outflow masses measured for Soil Layers 2 and 3 on the north-facing slope were generally

325 higher than those on the south-facing slope. For the drying tests using the soil mass of Soil Layers No. 2 and 3 on
 326 the north-facing slope, the given water outflow masses were 0.102 g/10 min and 0.131 g/10 min, respectively.
 327 However, the water outflow masses measured for the soil mass of Soil Layers No. 2 and 3 were 0.077 g/10 min and
 328 0.050 g/10 min, respectively, on the south-facing slope (Fig. 7a). For tests using the same layers of the soil mass in
 329 the wetting process, the water outflow masses measured were 0.051 g/10 min and 0.094 g/10 min on the north-facing
 330 slope, respectively, and 0.032 g/10 min and 0.027 g/10 min, respectively, on the south-facing slope (Fig. 7b). Overall,
 331 the permeability of the soil mass on the north-facing slope was higher than that on the south-facing slope. The same
 332 results were obtained when the saturated hydraulic conductivities of the soil layers were measured using the constant
 333 water head method (Table 1).



334
 335 **Fig. 7.** Mass of water outflow during the drying and wetting process: (a) drying tests, (b) wetting tests. The software
 336 automatically records the mass of water outflow 10 min each, so the x-axis starts from 10^0 .



337
 338 **Fig. 8.** Soil water curve obtained using the TRIM test: (a) Layer No. 2 on the south-facing slope, (b) Layer No. 3 on
 339 the south-facing slope, (c) Layer No. 2 on the north-facing slope, and (d) Layer No. 3 on the north-facing slope.

4.4.2 SWCC and HCF curves

341 The Soil Water Characteristic Curve (SWCC) and Hydraulic Conductivity Function (HCF) are critical for the
 342 analysis of water flow movement and mechanical behavior of unsaturated soil material. In this study, the Transient

343 Release and Imbibition Method (TRIM) for unsaturated hydraulic property measurement (Lu and Godt, 2013). The
 344 advantage of the TRIM method is that it combines physical experiments and calibration. It employs a relatively
 345 simple and reliable measurement of transient water content using an electronic balance to record the signature of
 346 transient unsaturated flow. It also takes advantage of the robust inverse modeling capability to simulate the physical
 347 process. The apparatus could accommodate both undisturbed and remolded samples. The results of this study were
 348 obtained using the Hydrus-1D code with the reverse modeling option, and the Levenberg–Marquardt non-linear
 349 optimization algorithm. This minimized the error between the results of the test and the simulation (Wayllace and
 350 Lu, 2012). Meanwhile, to ensure the uniqueness of the parameters, the algorithm repeatedly runs with different initial
 351 parameter estimates until it converges to obtain the same or similar results. The prediction results are then compared
 352 with the function curves of water flow and time obtained from the actual experiment so that they can be combined
 353 to meet certain accuracy requirements. In this experiment, the R square of the regression between the optimized
 354 predicted value and the observed value was greater than 0.99. The model constraint effect of the TRIM under two
 355 suction increment steps was better, and the parameters obtained by the inversion calculation were more accurate (Lu
 356 and Godt, 2013). Table 2 shows the soil parameters obtained using the Hydrus 1-D inversion.

357 Table 2 Parameters describing the Soil and Water Characteristic Curve (SWCC) and the Hydraulic Conductivity
 358 Function (HCF) from Hydrus 1-D

Parameters	Definition	South-facing slope		North-facing slope	
		Layer 2	Layer 3	Layer 2	Layer 3
θ_r	Residual moisture	0.0302	0.0278	0.0262	0.0268
θ_s^d	Saturated moisture	0.39	0.36	0.39	0.41
θ_s^w		0.36	0.38	0.39	0.42
α^d (kPa ⁻¹)	The inverse of the air-entry pressure head	0.0128	0.0117	0.0156	0.0141
α^w (kPa ⁻¹)		0.78	0.94	1.21	1.86
n^d	The pore size distribution parameter	1.49	1.39	1.57	1.27
n^w		1.63	1.85	1.43	1.18
K_s^d (cm/s)	Saturated hydraulic conductivity	1.52×10^{-4}	0.64×10^{-4}	3.76×10^{-4}	4.56×10^{-4}
K_s^w (cm/s)		9.58×10^{-2}	4.93×10^{-2}	4.10×10^{-1}	4.68×10^{-1}

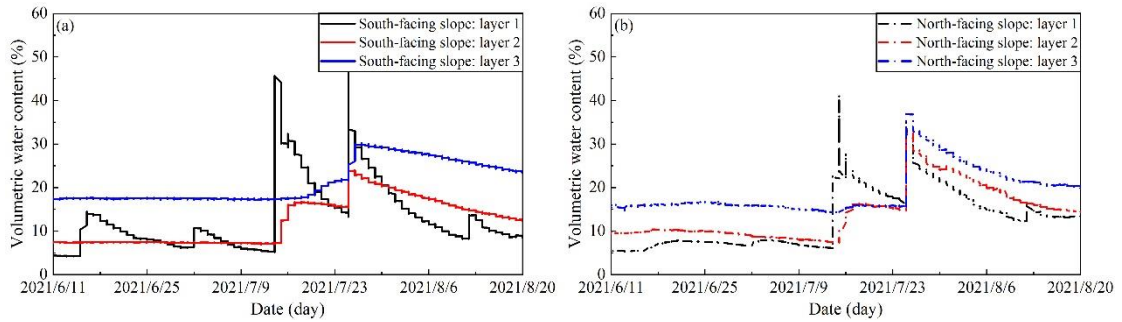
359 Notes: the superscript *d* and *w* indicate drying and wetting states.

360 Using these parameters, the SWCC and HCF curves of the soil mass at Soil Layers 2 and 3 on the north- and
 361 south-facing slopes can be drawn (Fig. 8). Air-entry pressure and residual water content are two important parameters
 362 that describe the hydrological and mechanical characteristics of the hillslope materials. The air-entry pressure
 363 represents the critical value at which air enters the saturated soil and starts to drain. For Soil Layer No. 2, the
 364 difference between the air entry values of the north- and south-facing slopes can reach 14.03 kPa (Figs. 8a and 8c).
 365 The residual water content and air-entry pressure of the south-facing slope were higher than those of the north-facing
 366 slope. For Soil Layer No. 3, the soil mass on the north-facing slope has the smallest air-entry pressure, which is 0.51
 367 times that of the air-entry pressure of the south-facing slope (Figs. 8b and 8d). The saturated hydraulic conductivities
 368 of Soil Layers No. 2 and 3 on the south-facing slope were lower than those on the north-facing slope in both the
 369 drying and wetting processes. The saturated hydraulic conductivity of the soil mass on the north-facing slope in the
 370 wetting test was one order of magnitude higher than that on the south-facing slope. In Table 1, the saturated
 371 permeability coefficient measured by the constant head test method also shows that the soil mass on north-facing

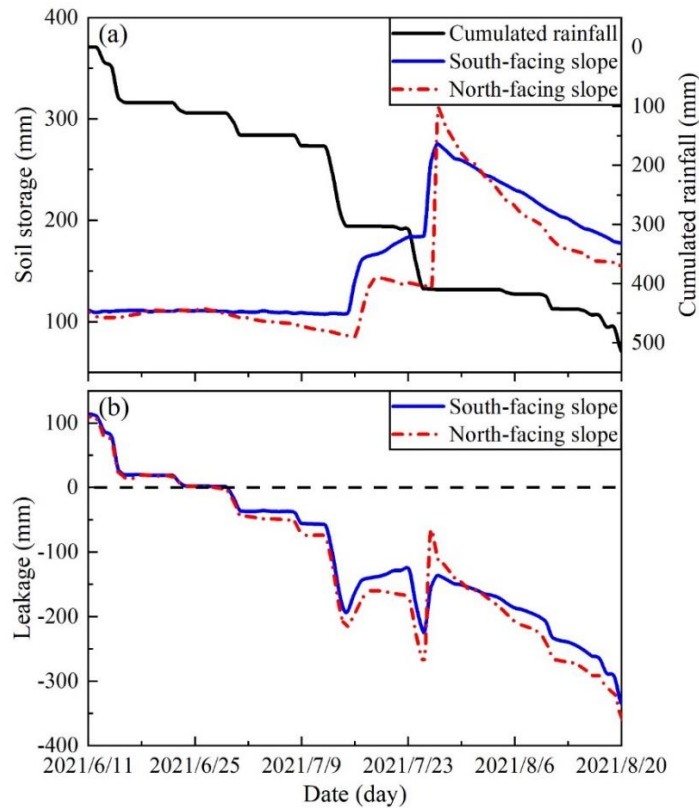
372 slope has higher permeability. These results suggest that it is more difficult for the soil mass on south-facing slope
 373 to absorb and drain water than the soil mass on the north-facing slope.

374 **4.5 Water storage and drainage**

375 To show the water storage during the rainfall process and the water drainage after the rainfall, the timely
 376 recorded soil moisture at various soil layers and the rainfall process during June 11 and August 20 were used (Figs.
 377 9a and 9b). In comparison, this is likely the most important finding, as it shows that the soil becomes nearly saturated
 378 on the south slope, but not on the north slope. This implies that the soil water on the south-facing slope has difficulty
 379 in draining water because of the presence of more fine grains and slow pore-water pressure dissipation. The stable
 380 soil moisture from Soil Layers No. 2 and 3 for both slopes may be attributed to the long dry seasons in the study
 381 area. The daily rainfall amount > 30 mm on July 9 and 23 resulted in an increase in soil moisture for all the slope
 382 layers.



383
 384 **Fig. 9.** Field monitored volumetric water content: (a) Soil moisture on the south-facing slope, and (b) soil moisture
 385 on the north-facing slope.



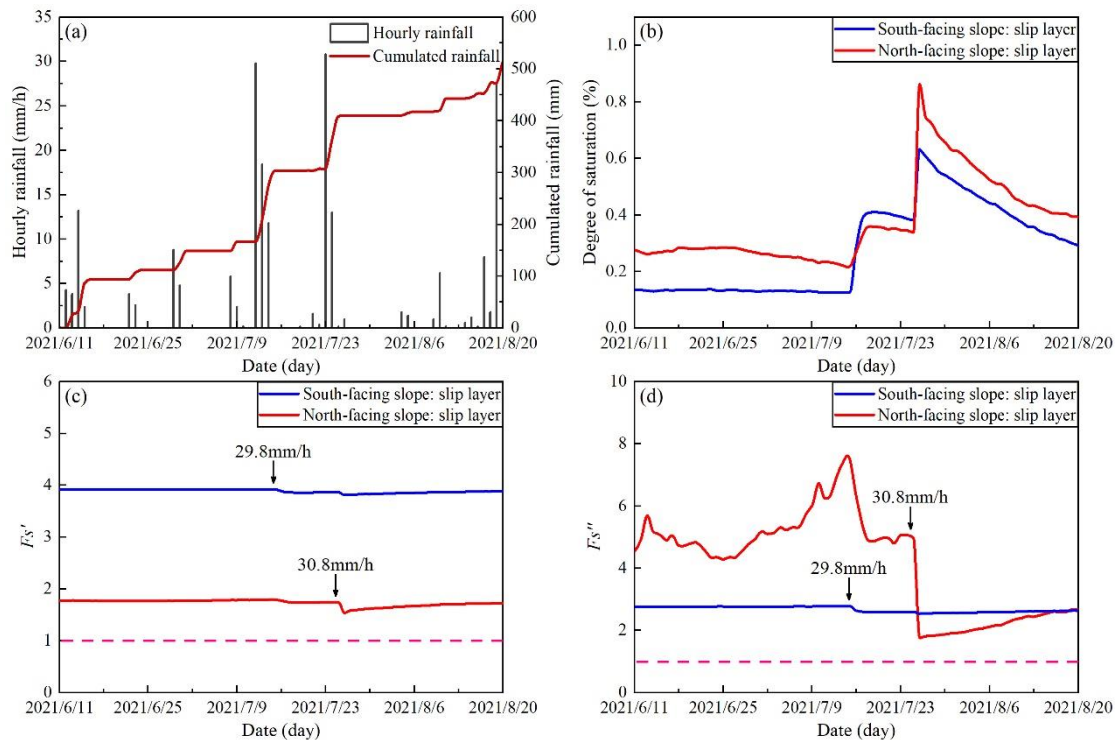
386
 387 **Fig. 10.** Seepage model of slope water storage and drainage. (a) soil water storage, (b) soil water drainage

388 Figure 10a shows that the storied water of the north- and south-facing slopes did not synchronously increase
 389 with accumulated precipitation. When the storied water rapidly increased, the increase in soil water storage of the

390 north-facing slope was greater than that of the south-facing slope. On July 26, a rainfall of 30.8 mm/h was recorded,
 391 and the water storage of the slope reached the peak. The peak of the water storage on the north-facing slope was
 392 higher than that of the south-facing slope. However, when the accumulated rainfall tends to be stable, that is, when
 393 the rainfall stops for a period, the decline rate of the soil water storage on the north-facing slope is substantially
 394 higher than that on the south-facing slope. The soil water storage of the south-facing slope was always higher than
 395 that of the north-facing slope during rainfall. During the drainage process, the seepage rate of the north-facing slope
 396 was greater than that of the south-facing slope (Fig. 10b). Therefore, the south-facing slope had a better water storage
 397 performance, and the north-facing slope had a higher drainage performance.

398 4.6 Stability fluctuation

399 In this study, the infinite slope model and the finite slope model were used to characterize the sensitivity of
 400 landslide triggering to determine the main mechanism of high landslide probability on south-facing slopes. The
 401 infinite slope model can be used to examine the transient stress changes caused by water entering the soil,
 402 emphasizing the differences in soil permeability (Lu and Likos, 2006; Lu and Godt, 2013). The finite slope model
 403 focuses on the cohesion of the base surface and lateral periphery of the ground landslide source body, as well as the
 404 influence of the additional lateral cohesion provided by the vegetation root system for the landslide (Schmidt et al.,
 405 2001; Dai et al., 2022).



406 **Fig. 11.** Change in slope stability fluctuation: (a) rainfall records, (b) degree of saturation, (c) stability of finite slope
 407 model, and (d) stability of infinite slope model. The pink dotted lines indicate the stability index equals to 1.0.
 408

409
 410 Figure 11a shows the rainfall records from June 11 to August 20, 2021. In general, the degree of saturation of
 411 the sliding layer on the south-facing slope was higher than that on the north-facing slope (Fig. 11b). In the finite
 412 model, the stability of the south-facing slope was always higher than that of the north-facing slope (Fig. 11c). In the
 413 infinite model, the stability of the north-facing slope was generally higher than that of the south-facing slope, and
 414 the stability of the north-facing slope fluctuated substantially (Fig. 11d). On July 26, a rainfall event with a maximum
 415 intensity of 30.8 mm/h resulted in a sudden decrease in stability. The estimated stability index of the north-facing
 416 slope decreased to become lower than that of the south-facing slope and then increased afterwards. Although the soil

417 moisture of the south-facing slope increased substantially during the rainfall event on July 16, the stability fluctuation
418 was relatively small. This may be related to the relatively strong effective cohesion and smaller pore structure. In
419 finite slope model, the results have shown that the south-facing slope has a relatively high stability. However, this
420 result contradicts to the high landslide density on the south-facing slope in the study area. In fact, the finite slope
421 model does not consider suction stress, and the effective cohesion of hillslope materials mainly affects the stability
422 result. In contrast, the results of the infinite slope model asserts that the state of the stress of the soil or regolith is
423 modified by infiltration and changes in soil matrix suction. Furthermore, the fluctuation in fig. 11d also proves that
424 the role of infiltration of water into shallow soils and the subsequent pore-water pressure response at depth is critical
425 to the understanding the transient conditions that lead to shallow slope failure, because the stability fluctuation
426 amplitude of the south-facing hillslope was smaller than that of the north-facing hillslope. This indicated that the
427 water movement on the south-facing slope was less active than that of the north-facing slope. Therefore, in the study
428 area, the change in soil suction stress was more sensitive to slope stability than the change in root soil cohesion. The
429 change in soil permeability caused by differential weathering of the bedrock could be responsible for aspect-
430 dependent landslide initiation in the study area.

431 **5 Discussion**

432 The strong propensity for landslides in some arid environments in the Northern Hemisphere is scientifically
433 interesting, and some researchers have highlighted the contribution of plant roots. This finding is to be expected in
434 the future in other mountain regions, where water is a limiting factor for local system sustainability. In the Colorado
435 Frontal range, McGuire et al. (2016) found that the apparent cohesion supplied by roots was responsible for the
436 connection observed between landslide distribution and slope aspect (Ebel, 2015; Rengers et al., 2016). In the study
437 area, Li et al. (2021) also found that plant roots may explain the connection observed between vegetation cover and
438 landslide probability for the entire study area. Dai et al. (2022) found that a strong root network and high saturated
439 hydraulic conductivity may promote the $A-S$ condition of shallow landslides. On the Loess Plateau in China, some
440 researchers have observed that the strong propensity for shallow landslide initiation is closely related to the present-
441 day tree density, and plant roots do not penetrate over the failure plane (Guo et al., 2020; Deng et al., 2022). However,
442 the strong propensity for shallow landslides on north- and south-facing slopes cannot be attributed to plant roots,
443 because the artificial vegetation on both slopes is the same. Conversely, these observations could be the result of the
444 soil hydraulic and mechanical properties from differential weathering.

445 This study has contributed to knowledge of the effect of differential weathering on aspect-dependent landslide
446 initiation from the perspective of soil hydraulic properties, in addition to the mechanical and hydrological effects of
447 plant roots. Except for the strong propensity for a high number of landslides, shallow landslides on south-facing
448 slopes have exhibited larger areas and greater widths than those on the north-facing slopes (Fig. 2). This may be
449 attributed to the fact that the slow dissipation of excessive pore-water pressure because widespread liquefaction may
450 cause extend the landslide scale. For the thinner slip layer of landslides on south-facing slope, it may result from
451 differential weathering, because the theoretical maximum or maximum slip layer for strong-cohesive slope should
452 be larger than weak-cohesive slope at given slope (Iida, 1999; D'Odorico and Fagherazzi, 2003). One of the reasons
453 may be that cohesive soil mass often hold tight together to displace downslope owing to the strength loss. The
454 relatively weak-cohesive soil mass often loosens to displace downslope, with the slip layer close to the boundary
455 between soil mass and bedrock underneath. However, a stronger effective cohesion tends to promote the $A-S$
456 conditions of shallow landslides. A larger up-slope contributing area or steeper gradient is required to trigger slope
457 failure. Figure 3 shows that some shallow landslides on south-facing slopes fail at lower upslope contributing areas.
458 Therefore, soil hydraulic property-related factors, such as the rising or dissipation of pore-water pressure, water
459 storage, and drainage, may contribute to the phenomena observed.

460 The saturated hydraulic conductivities obtained by the constant water head and TRIM methods coincide, which
461 demonstrates that the hillslope material on the north-facing slope has a larger water infiltration (Tables 1 and 2).
462 However, the difference between K_s^d and K_s^w is strikingly high and the K_s^d is smaller. Although the Trim test in this
463 work measures the permeability of soil matrix, the influence of other factors, such as the soil development and
464 weathering, preferential flow pathway and macro pore, cannot be ignored (Lohse and Dietrich, 2005; Maier et al.,
465 2020), and the contribution of such influence on the permeability rate cannot be evaluated at present. The results of
466 the stability analysis using the finite and infinite models imply that the failure potential of slides on a north-facing
467 slope is lower than that on a south-facing slope, because the stability index of south-facing slope is always close to
468 1.0. These differences imply that slope failures on a north-facing slope may only occur under intensive rainfall
469 conditions or by a combination of prolonged antecedent precipitation and short duration intensive rainfall. For
470 potential failures on south-facing slopes, the combination of prolonged antecedent precipitation and short duration
471 intensive rainfall should be a potential trigger owing to the low hydraulic conductivity and pore-water pressure
472 dissipation. This study highlights the role of hydraulic properties in landslide occurrence. Although the south- and
473 north-facing slopes are underlain by granite, the physical properties of hillslope materials such as excessive pore-
474 water pressure, strength of sliding mass, soil water storage, and leakage are significantly different. One of the
475 possible limitations of this work lies in that the representativeness of the moisture observation and the uncertainty.
476 Considering the multiple factors influencing landslides, the study area is selected with same bedrock underneath and
477 similar plant species. Then, the moisture observation sites were selected on condition that similar soil profile,
478 landscape with majority of landslides and the common topographical conditions. Therefore, this finding cannot be
479 random because the study area has been selected on the condition that it is relatively far from the northern and eastern
480 areas where local soils are predominantly loess deposits, and the study areas of Li et al. (2021) and Dai (2022), where
481 the bedrock underneath differs substantially. The main purpose of this work is to elucidate the reason for aspect-
482 dependent landslide initiation from the perspective of soil hydraulic properties. These differences result from
483 differential weathering owing to the amount of direct sunlight. Other methods such as numerical or relative dating
484 methods and preferential flow in the macropore distribution could provide new evidence for such observations.

485 **6 Conclusion**

486 Previous research on the strong propensity for shallow landslides on south-facing slopes over north-facing
487 slopes has highlighted the role of plant roots. In a localized area with the same vegetation including plant roots, they
488 do not penetrate the failure layer. Such overwhelming landslide phenomenon cannot be attributed to plant roots and
489 may result from the differential weathering of bedrock under the influence of hydrothermal conditions. In this study,
490 we jointly explained the soil hydraulic properties from physical and mechanical properties, pore-water pressure,
491 unsaturated hydraulic conductivity, water storage and drainage, and slope stability fluctuation during monitoring,
492 and studied landslide initiation related to slope direction. The following conclusions were drawn:

493 (1) In terms of soil physical and mechanical properties on both slopes, the soil masses on the south-facing slope
494 have higher silt content than those on the north-facing slope. The effective cohesion of the soil mass on the south-
495 facing slope was higher than that on the north-facing slope, while the effective frictional angle was smaller.

496 (2) The results of the GDS tests showed that the dissipation rate of pore-water pressure for soil mass on the
497 south-facing slope was substantially lower than that on the north-facing slope. Higher effective cohesion and slower
498 pore-water pressure dissipation may result in a larger basal area for shallow landslides on south-facing slopes.

499 (3) The soil mass on the south-facing slope had a higher residual water content and air entry pressure, and a
500 lower saturated hydraulic conductivity than that of the north-facing slope. For water storage and drainage
501 performance, the storied water from the south-facing slope was higher than that of the north-facing slope, while the
502 north-facing slope had a higher leakage rate. The results of the stability analysis based on the finite and infinite

503 models show that the infinite slope model may be suitable for elucidating aspect-dependent landslide distribution in
504 the study area.

505 **Acknowledgements**

506 This study was supported by the State Key Program of National Natural Science of China (Grant No. 42130701),
507 the National Nature Science Foundation of China (42177309), and the Fundamental Research Funds for the Central
508 Universities (Grant No. 2018BLCB03). The authors sincerely thank the contributions of other colleges, including
509 Muyang Li, Zhisheng Dai, Lv Miao, Lijuan Wang, and Jiayong Deng, for their previous work near the study area.

510 **Code/Data availability**

511 The raw/processed data in this work cannot be shared at this time, because the data also form part of an ongoing
512 study.

513 **Author contributions**

514 Professor Ma Chao found a strong propensity for shallow landslide initiation on south-facing hillslopes in the study
515 area and launched a research proposal. Miss Yanglin Guo completed the sampling collection and indoor tests.

516 **Competing interests**

517 All authors have declared that there were no conflicts of interests and competing interests.

518 **References**

- 519 [1] Bierman, P. R., Montgomery, D. R.: Key Concepts in Geomorphology, W.H. Freeman, 2014.
520 [2] Birkeland, P. W.: Soils and Geomorphology, New York: Oxford University Press, 1999.
521 [3] Bogaard, T. A., Greco, R.: Landslide hydrology: from hydrology to pore pressure, Wiley Interdiscip. Rev.
522 Water, 3, 439-459, <https://doi.org/10.1002/wat2.1126>, 2016.
523 [4] Coe, J. A., Kean, J. W., Godt, J. W., Baum, R. L., Jones, E. S., Gochis, D. J., Anderson, G. S.: New insights
524 into debris-flow hazards from an extraordinary event in the Colorado front range, GSA Today, 24, 4-10,
525 <https://doi.org/10.1130/GSATG214A.1>, 2014.
526 [5] D' Odorico, P., Fagherazzi, S.: A probabilistic model of rainfall-triggered shallow landslides in hollows: A
527 long-term analysis, Water Resour. Res., 39(9), 1262, <https://doi.org/10.1029/2002WR001595>, 2003.
528 [6] Dai, Z. S., Ma, C., Miao, L., Li, M. Y., Wu, J. L. and Wang, X. H.: Initiation conditions of shallow landslides
529 in two man-made forests and back estimation of the possible rainfall threshold, Landslides, 19, 1031-1044,
530 <https://doi.org/10.1007/s10346-021-01823-1>, 2022.
531 [7] Deng, J. Y., Ma, C., and Zhang, Y.: Shallow landslide characteristics and its response to vegetation by example
532 of July 2013, extreme rainstorm, Central Loess Plateau, China. Bulletin of Engineering Geology and the
533 Environment, 81-100, <https://doi.org/10.1007/s10064-022-02606-1>, 2022.
534 [8] Ebel, B. A., Rengers, F. K., Tucker, G. E.: Aspect-dependent soil saturation and insight into debris-flow
535 initiation during extreme rainfall in the Colorado front range, Geology, 43, 659-662,
536 <https://doi.org/10.1130/G36741.1>, 2015.
537 [9] Fu, B. J., Wang, Y. F., Lu, Y. H., He, C. S., Chen, L. D., Song, C. J.: The effects of land-use combinations on
538 soil erosion: a case study in the Loess Plateau of China, Prog. Phys. Geo., 33, 793-804,
539 <https://doi.org/10.1177/0309133309350264>, 2009.
540 [10] Fu, B. P.: Mountain climate, Science Press, 1983 (in Chinese)
541 [11] Geroy, I. J., Gribb, M. M., Marshall, H. P., Chandler, D. G., Benner, S. G., McNamara, J. P.: Aspect influences
542 on soil water retention and storage, Hydrological Processes, 25, 3836-3842, <https://doi.org/10.1002/hyp.8281>,
543 2011.

- 544 [12] Godt, J. W., Baum, R. L., and Lu, N.: Landsliding in partially saturated materials. *Geophys. Res. Lett.*, 36,
545 L02403, <https://doi.org/10.1029/2008GL035996>, 2009.
- 546 [13] Guo, F. Y., Meng, X. Y., Li, Z. H., Xie, Z. T., Chen, G., He, Y. F.: Characteristics and causes of assembled
547 geo-hazards induced by the rainstorm on 25th July 2013 in Tianshui City, Gansu, China, *Mt. Res.*, 33, 100-
548 107, 2015 (in Chinese)
- 549 [14] Guo, W. Z., Chen, Z. X., Wang, W. L., Gao, W. W., Guo, M. M., Kang, H. L., Li, P. F., Wang, W. X., Zhao,
550 M.: Telling a different story: The promote role of vegetation in the initiation of shallow landslides during
551 rainfall on the Chinese Loess Plateau, *Geomorphology*, 350, 106879,
552 <https://doi.org/10.1016/j.geomorph.2019.106879>, 2020.
- 553 [15] Hungr, O., McDougall, S., Bovis, M.: Entrainment of material by debris flows. In: *Debris-flow Hazards and*
554 *Related Phenomena*. Springer Praxis Books. Springer, Berlin, Heidelberg. [https://doi.org/10.1007/3-540-](https://doi.org/10.1007/3-540-27129-5_7)
555 [27129-5_7](https://doi.org/10.1007/3-540-27129-5_7), 2005.
- 556 [16] Heimsath, A.M., Deitrich, W.E., Nishizumi, K., Frinkel, R.C.: The soil production function and landscape
557 equilibrium, *Nature*, 388, 358-361, 1997. <https://doi.org/10.1038/41056>.
- 558 [17] Iverson, R. M., LaHusen, R. G.: Dynamic pore-pressure fluctuations in rapidly shearing granular materials,
559 *Science*, 246, 796-799, <https://doi.org/10.1126/science.246.4931.796>, 1989.
- 560 [18] Iverson, R. M., Reid, M. E., LaHusen, R. G.: Debris-flow mobilization from landslides, *Annu. Rev. Earth*
561 *Planet. Sci.*, 25, 85-138, <https://doi.org/10.1146/annurev.earth.25.1.85>, 1997.
- 562 [19] Iida, T.: A stochastic hydro-geomorphological model for shallow landsliding due to rainstorm. *Catena*, 34(3-
563 4), 293-313, [https://doi.org/10.1016/S0341-8162\(98\)00093-9](https://doi.org/10.1016/S0341-8162(98)00093-9), 1999.
- 564 [20] Iverson, R.M., Reid, M.E., Logan, M., Lahusen, R.G., Godt, J.W., Griswold, J.P.: Positive feedback and
565 momentum growth during debris-flow entrainment of wet bed sediment, *Nature. Geosci.*, 4(2), 116–121,
566 <https://doi.org/10.1038/ngeo1040>, 2011.
- 567 [21] Lee, E., Kim, S. Seasonal and spatial characterization of soil moisture and soil water tension in a steep hillslope,
568 *J. Hydrol.*, 568, 676-685, <https://doi.org/10.1016/j.jhydrol.2018.11.027>, 2019.
- 569 [22] Li, M. Y., Ma, C., Du, C., Yang, W. T., Lyu, L. Q., Wang, X. H.: Landslide response to vegetation by example
570 of July 25-26, 2013, extreme rainstorm, Tianshui, Gansu Province, China, *Bull. Eng. Geol. Environ.*, 80, 751-
571 764, <https://doi.org/10.1016/10.1007/s10064-020-02000-9>, 2021.
- 572 [23] Lu, N., and Godt, J. W.: *Hillslope hydrology and stability*, Cambridge Univ. Press, Cambridge, UK, 2013.
- 573 [24] Lu, N., and Likos, W. J.: Suction stress characteristic of unsaturated soils, *J. Geotech. Geoenviron. Eng.*, 132,
574 131-142, [http://doi.org/10.1061/\(ASCE\)1090-0241\(2006\)132:2\(131\)](http://doi.org/10.1061/(ASCE)1090-0241(2006)132:2(131)), 2006.
- 575 [25] Lohse, K. A., Dietrich, W. E.: Contrasting effects of soil development on hydrological properties and flow
576 paths, *Water Resour. Res.*, 41, 1–17, <https://doi.org/10.1029/2004WR003403>, 2005.
- 577 [26] Maier, F., van Meerveld, I., Greinwald, K., Gebauer, T., Lustenberger, F., Hartmann, A., Musso, A.: Effects
578 of soil and vegetation development on surface hydrological properties of moraines in the Swiss Alps, *Catena*,
579 187, 104353, <https://doi.org/10.1016/j.catena.2019.104353>, 2020.
- 580 [27] McGuire, L. A., Rengers, F. K., Kean, J. W., Coe, J. A., Mirus, B. B., Baum, R. L., Godt, J. W.: Elucidating
581 the role of vegetation in the initiation of rainfall-induced shallow landslides: insights from an extreme rainfall
582 event in the Colorado front range, *Geophys. Res. Lett.*, 43, 9084-9092, <https://doi.org/10.1002/2016GL070741>,
583 2016.
- 584 [28] Montgomery, D. R., Dietrich, W. E.: Landscape dissection and drainage area-slope thresholds, In: Kirkby MJ
585 (ed) *Process models and theoretical geomorphology*, John Wiley, Hoboken, N. J., pp: 221-246, 1994.
- 586 [29] Mualem, Y.: Hysteretical models for prediction of the hydraulic conductivity of unsaturated porous media,
587 *Water Resour. Res.*, 12, 1248-1254, <https://doi.org/10.1029/WR012i006p01248>, 1976.

- 588 [30] Rengers, F. K., McGuire, L. A., Coe, J. A., Kean, J. W., Baum, R. L., Staley, D. M., Godt, J. W.: The influence
589 of vegetation on debris-flow initiation during extreme rainfall in the northern Colorado front range, *Geology*,
590 44, 823-826, <http://doi.org/10.1130/G38096.1>, 2016.
- 591 [31] Sassa, K.: The mechanism starting liquefied landslides and debris flows. *Proceedings of 4th International*
592 *Symposium on Landslides*, Toronto, Canada, vol. 2, pp. 349-354, 1984.
- 593 [32] Schmidt, K. M., Roering, J. J., Stock, J. D., Dietrich, W. E., Montgomery, D. R., Schaub, T.: The variability
594 of root cohesion as an influence on shallow landslide susceptibility in the Oregon Coast Range, *Can. Geotech.*,
595 38, 995-1024, <http://doi.org/10.1139/cgi-38-5-995>, 2001.
- 596 [33] Schwinning, S.: The ecohydrology of roots in rocks, *Ecohydrology: Ecosystems, land and water process*
597 *interactions*, *Ecohydrology*, 3, 238-245, <https://doi.org/10.1002/eco.134>, 2010.
- 598 [34] Terzaghi, K.: Mechanism of landslides. In: Paige, S. (Ed.), *Application of Geology to Engineering Practice*
599 *(Berkey Volume)*. Geological Society of America, New York, pp. 83-123, 1950.
- 600 [35] Timilsina, S., Niemann, J. D., Rathburn, S. L., Rengers, F. K., Nelson, P. A.: Modeling hydrologic processes
601 associated with soil saturation and debris flow initiation during the September 2013 storm, *Colorado Front*
602 *Range, Landslides*, 18, 1741-1759, <https://doi.org/10.1007/s10346-020-01582-5>, 2021.
- 603 [36] Van Genuchten, M. T.: A closed-form equation for predicting the hydraulic conductivity of unsaturated soils,
604 *Soil Sci. Soc. Am. J.*, 44, 892-898, <https://doi.org/10.2136/sssaj1980.03615995004400050002x>, 1980.
- 605 [37] Wang, C. Y.: Study on the relationship between aspect and slope stability, Dissertation, Kunming University
606 of Science and Technology, 2008 (in Chinese).
- 607 [38] Wang, G. H., Sassa, K.: Pore-pressure generation and movement of rainfall-induced landslides: effects of grain
608 size and fine-particle content, *Eng. Geol.*, 69, 109-125, [https://doi.org/10.1016/S0013-7952\(02\)00268-5](https://doi.org/10.1016/S0013-7952(02)00268-5), 2003.
- 609 [39] Wang, X. H., Ma, C., Wang, Y. Q., Wang, Y. J., Li, T., Dai, Z. S., Li, M. Y.: Effect of root architecture on
610 rainfall threshold for slope stability: variabilities in saturated hydraulic conductivity and strength of root-soil
611 composite, *Landslides*, 17, 1965-1977, <https://doi.org/10.1007/s10346-020-01422-6>, 2020.
- 612 [40] Watakabe, T., Matsushi, Y.: Lithological controls on hydrological processes that trigger shallow landslides:
613 Observations from granite and hornfels hillslopes in Hiroshima, Japan, *Catena*, 180: 55-68,
614 <https://doi.org/10.1016/j.catena.2019.04.010>, 2019
- 615 [41] Wayllace, A., Lu, N.: A transient water release and imbibitions method for rapidly measuring wetting and
616 drying soil water retention and hydraulic conductivity functions. *Geotech. Test. J.*, 35, 1-15, 2012.
- 617 [42] Yu, G. Q., Zhang, M. S., Hu, W.: Analysis on the development characteristics and hydrodynamic conditions
618 for massive debris flow in Tianshui, *Northwest Geol.*, 47, 185-191, 2014 (in Chinese)